The Astrophysical Journal, 933:220 (13pp), 2022 July 10 https://doi.org/10.3847/1538-4357/ac6c8e
© 2022. The Author(s). Published by the American Astronomical Society.
OPEN ACCESS

Growth of Outward Propagating Fast-magnetosonic/Whistler Waves in the Inner Heliosphere Observed by Parker Solar Probe

Jiansen He[1], Ying Wang[1], Xingyu Zhu[1], Die Duan[1], Daniel Verscharen[2], and Guoqing Zhao[3]
[1] School of Earth and Space Sciences, Peking University, Beijing, 100871, People's Republic of China; jshept@pku.edu.cn
[2] Mullard Space Science Laboratory, University College London, Dorking RH5 6NT, UK
[3] Institute of Space Physics, Luoyang Normal University, Luoyang, People's Republic of China
Received 2021 September 1; revised 2022 April 25; accepted 2022 May 2; published 2022 July 15

Abstract

The solar wind in the inner heliosphere has been observed by Parker Solar Probe (PSP) to exhibit abundant wave activities. The cyclotron wave modes responding to ions or electrons are among the most crucial wave components. However, their origin and evolution in the inner heliosphere close to the Sun remains a mystery. Specifically, it remains unknown whether it is an emitted signal from the solar atmosphere or an eigenmode growing locally in the heliosphere due to plasma instability. To address and resolve this controversy, we must investigate the key quantity of the energy change rate of the wave mode. We develop a new technique to measure the energy change rate of plasma waves, and apply this technique to the wave electromagnetic fields measured by PSP. We provide the wave Poynting flux in the solar wind frame, identify the wave nature to be the outward propagating fast-magnetosonic/whistler wave mode instead of the sunward propagating waves. We provide the first evidence for growth of the fast-magnetosonic/whistler wave mode in the inner heliosphere based on the derived spectra of the real and imaginary parts of the wave frequencies. The energy change rate rises and stays at a positive level in the same wavenumber range as the bumps of the electromagnetic field power spectral densities, clearly manifesting that the observed fast-magnetosonic/whistler waves are locally growing to a large amplitude.

Unified Astronomy Thesaurus concepts: Solar wind (1534); Interplanetary turbulence (830)

1. Introduction

Waves are essential channels of energy conversion in various plasma systems. Particularly for the waves at kinetic scales, wave-particle interactions play a crucial role in modulating the particles velocity distribution, leading to the energization/cooling of plasmas, as well as the kinetic energy transfer between parallel and perpendicular degrees of freedom (Hellinger et al. 2006; Marsch 2006; He et al. 2015b; Ruan et al. 2016; Howes et al. 2017; Yoon 2017; Klein et al. 2018; Verscharen et al. 2019; Duan et al. 2020; Verniero et al. 2020; Zhao et al. 2020). Regarding space plasmas in the heliosphere, the situation is more complicated. Various wave modes exist: electromagnetic wave modes (e.g., Alfvén-cyclotron waves, whistler waves) (Jian et al. 2009; He et al. 2011; Boardsen et al. 2015; Narita 2018; Zhao et al. 2018; Woodham et al. 2019; Bowen et al. 2020c; Jagarlamudi et al. 2021; Shi et al. 2021; Zhao et al. 2021), electrostatic wave modes (e.g., ion-acoustic waves, Langmuir waves) (Zhu et al. 2019; Mozer et al. 2020b), and hybrid wave modes (e.g., quasi-perpendicular kinetic Alfvén waves) (Bale et al. 2005; Sahraoui et al. 2009; He et al. 2012; Salem et al. 2012; Chen et al. 2013; Huang et al. 2020). Observations reveal propagation directions to be anti-sunward or sunward, quasi-parallel or quasi-perpendicular with respect to the local-background magnetic field direction. The polarization of the fluctuating vectors (e.g., $\delta\boldsymbol{B}$, $\delta\boldsymbol{E}$, and $\delta\boldsymbol{V}$ for the disturbed magnetic, electric, and velocity field vectors, respectively) can be quasi-linear or quasi-circular with left- or right-handedness. It is also desired to distinguish whether the observed waves are dissipative damping or stimulative growing. Therefore, a thorough diagnosis of the kinetic waves in space plasmas, including the solar wind, is undoubtedly a challenging task.

The fluctuating magnetic field can be helpful in determining the propagation, but a 180° ambiguity remains. Since the magnetic field is a solenoidal vector field, the wave magnetic field ($\delta\boldsymbol{B}$) cannot have a component oscillating along the wavevector direction. In this work, we will apply this feature of magnetic field fluctuations to the diagnosis of waves at ion kinetic scales. This feature of the oscillation direction provides a basis for diagnosing the propagation direction. Therefore, approximating the wavevector direction with the minimum variance direction has become one of the main principles when developing wavevector diagnosis methods, such as the MVA Minimum Variance Analysis (MVA) method based on time series (Sonnerup & Cahill 1967), or the Singular Value Decomposition (SVD) method based on the spectrum or dynamic spectrum (Santolík et al. 2003). According to these methods, we can preliminarily diagnose whether the wave encountered by a spacecraft has a quasi-parallel propagation or a quasi-perpendicular propagation. For example, we often see that with decreasing wavelength the magnetic compressibility becomes more significant, and the corresponding θ_{kB_0} becomes larger (He et al. 2015a). One of the reasons for this change in behavior is the transformation from magnetohydrodynamic (MHD) Alfvén waves to kinetic Alfvén waves with decreasing scales. However, single-satellite magnetic field measurements cannot solve the problem of the 180° ambiguity of the propagation angle. So, these measurements are unable to judge the real propagation direction of the wave, and hence unable to accurately diagnose the nature of wave mode. To unambiguously identify the wave propagation direction, there are two possible solutions: (1) the time delay analysis based on multi-satellite constellation measurements (Gershman et al. 2017); (2)

Original content from this work may be used under the terms of the Creative Commons Attribution 4.0 licence. Any further distribution of this work must maintain attribution to the author(s) and the title of the work, journal citation and DOI.

the consideration of more physical measurements (such as wave electric field, e.g., measured from *Magnetospheric MultiScale mission* (MMS; He et al. 2019, 2020).

The fluctuating electric field is another crucial variable for wave diagnosis (Mozer & Chen 2013; He et al. 2020). Only when the wave electric and magnetic fields are measured simultaneously, can the wave electromagnetic energy-flux density, that is, the Poynting flux density, be calculated. However, the measurement and calibration of the electric field are more complicated than of the magnetic field due to Debye shielding and the photoelectric effect, which bring a significant challenge to the accurate measurement of the electric field. Fortunately, the number density of the solar wind measured by PSP is two orders of magnitude higher than that of the near-Earth solar wind, and the Debye sphere is thus one order of magnitude smaller, making shorter electric-field antennas feasible (Bale et al. 2016; Mozer et al. 2020a). Furthermore, the PSP antenna's geometric configuration leaves the potential measurement at the four ends (U_1, U_2, U_3, and U_4) unaffected by the wake of the spacecraft. In this way, in the absence of physical adverse factors, the main task for the data analysis is the careful calibration of the electric field. The convection electric field at MHD scales can be used as the benchmark electric field to calibrate the electric field based on multipoint potential measurements (Mozer et al. 2020a). Based on the magnetic field's frozen-in condition at MHD scales, the convection electric field can be approximated by the opposite of the cross product of the fluid velocity and magnetic field vectors ($\boldsymbol{E} \sim -\boldsymbol{V} \times \boldsymbol{B}$). In the ideal case, if the antenna pairs are perfectly configured and long enough to avoid the spacecraft sheath effect, the calibration coefficients obtained at MHD scales can be extended to the electric field calibration at kinetic scales. However, in reality, the antenna pairs are limited by their finite length and non-perfect configuration, calling attention to the scale dependence of calibration coefficients. For example, one needs to be cautious when trying to adopt the calibration coefficients at MHD scales to the electric field calibration at electron kinetic scales, which are much smaller than MHD scales. Nevertheless, it is an acceptable compromise scheme for the electric field at ion kinetic scales close to MHD scales to calibrate it using the calibration coefficients at MHD scales. Please note that the calibrated ion-scale electric field does not need to obey the frozen-in condition as that at MHD scales. Suppose there is a measurement of electron fluid velocity at ion kinetic scales. In that case, it is better to calibrate from potential to electric field by using the approximation of $\boldsymbol{E} \sim -\boldsymbol{V}_e \times \boldsymbol{B}$ at ion kinetic scales. Based on the time series of electric and magnetic fields, it is found that the magnitude of the Poynting vector in a switchback structure is larger than that outside (Mozer et al. 2020a). The reason is that the outflow velocity inside the structure is larger, and so is the angle between the outflow velocity and the magnetic field. Besides, the propagation speed of the kinetic wave's Poynting vector in the heliographic inertial (HGI) reference frame is larger than the solar wind flow speed, suggesting that the wave events under study propagate away from the Sun (Bowen et al. 2020a).

The origin of kinetic-scale fluctuations in the solar wind is a controversial topic of research. There are two different views on this issue. (1) One view is that the wave fluctuations are emitted from the solar atmosphere and cascade from the MHD scales to the kinetic scales during their journey of outward propagation (He et al. 2009; Cranmer et al. 2015; Yang et al. 2017; Chandran & Perez 2019; He et al. 2021). (2) The other view is that the kinetic-scale waves are produced locally in the interplanetary space due to some plasma instability (Jian et al. 2014; Wicks et al. 2016; Jiansen et al. 2018; Zhao et al. 2019; Verniero et al. 2020). Because the cascade of the Alfvén turbulence preferentially creates anisotropy with $k_\perp \gg k_\parallel$, the quasi-perpendicular propagation of kinetic Alfvén waves may be generated by a cascade along with the outward propagation of MHD waves. The mechanism of origin is especially unclear for quasi-parallel kinetic waves (such as ion-cyclotron waves or whistler waves). However, due to the frequent existence of spectral peaks, it is generally speculated that these waves are related to the excitation by local instability. In addition, the thermal anisotropy of protons, the beam structures in protons and other ions, and the heat flux caused by the strahl component of the solar wind electrons may cause instabilities in various plasma states. However, previous studies, which are mainly based on the prediction from linear theory, have not provided direct evidence for the time-varying growth of solar wind kinetic waves.

Therefore, it is one of the cutting-edge frontiers to study and provide evidence of the time-varying evolution (growth or dissipation) of wave events. Quasi-parallel kinetic waves (such as ion-cyclotron waves) were once considered an important energy source for solar wind heating. The dissipation of quasi-perpendicular kinetic Alfvén waves is also an effective way to heat the solar wind. These viewpoints need to be proved by the direct observation of the dissipation rate spectrum, but the dissipation rate spectrum has been unexplored for a long time. Recently, based on the detection of electromagnetic field and plasma in the magnetosheath turbulence by MMS, the measurement method of the dissipation rate spectrum was proposed (He et al. 2019). The dissipation rate spectra of ion-cyclotron waves (mainly in the perpendicular direction) and kinetic Alfvén waves (mainly in the parallel direction) in magnetosheath turbulence are measured (He et al. 2019, 2020). The existence of linear instability was inferred by applying plasma wave theory to PSP observations of proton distributions with one or two components (Klein et al. 2021). However, the observational growth rate spectrum of an excited instability has yet to be reported. Although the trivial energy transfer rate from fields to particles as compared with the energy-flux density supports local generation scenario of cyclotron waves (Vech et al. 2021), the direct measurement of the wave growth in the inner heliosphere and the details of the associated growth rate spectrum are still unresolved.

2. Method of Wave Diagnosis

2.1. Calibration of Electric Field

The FIELDS antennas are not geometrically orthogonal. The V_1-V_2 antennas are located at an angle of 55° from the spacecraft X-axis, while the V_3-V_4 antennas are at an angle of 40°. So the angle between the cross dipoles is 95° (or 85°). The starting point for our data analysis is the Digital Fields Board (DFB) differential voltage waveform data of level 2 and the data version of version 3. This data set has already been corrected for the non-orthogonality by rotating into the spacecraft coordinates from the sensor coordinates. Therefore, we do not need to further consider the non-orthogonality in our analysis. Here, we name the invoked observational data as U_X^*

and U_Y^* to represent the nominal differential voltages along the X and Y axes in the spacecraft coordinates, which needs further correction for spacecraft sheath effect before comparing with the inductive electric field from solar wind plasma flow.

Since the magnetic frozen-in condition holds at MHD scales, the electric field due to convection ($\boldsymbol{E} = -\boldsymbol{V} \times \boldsymbol{B}$) can be used as the benchmark electric field at MHD scales in both time and frequency for calibration. We note that a better approximation of the electric field due to convection would be $\boldsymbol{E} = -\boldsymbol{V}_e \times \boldsymbol{B}$, where $\boldsymbol{V}_e$ is the bulk electron velocity, especially when looking at the electric-field variations at scales comparable to or smaller than the ion inertial length. The MHD-scale wavenumber has an upper limit at the characteristic ion kinetic scales (e.g., $k\rho_i \sim 1$ and $kd_i \sim 1$). In the present study, the Doppler-shifted frequency in the spacecraft reference frame for the wavenumber $k\rho_i \sim 1$ and $kd_i \sim 1$ is estimated to be about 7.5 and 4.0 Hz, corresponding to the timescales of 0.13 and 0.25 s, respectively.

The calibration of the electric field radial component E_R is difficult and much more complicated than that of the tangential and normal components E_T and E_N in RTN coordinates, since the measurement of the potential at the V_5 voltage sensor related to E_R is in the wake of the PSP spacecraft and subject to the wake effect (Mozer et al. 2020a). The Z-axis of the PSP spacecraft coordinates is in the sunward direction (i.e., the $-R$ direction in the RTN coordinates during the PSP perihelion encounter). During the perihelion phase, the differences between the voltage potentials at the antenna sensors of V_1, V_2, V_3, and V_4 are related to the electric field components in the 2D $T-N$ plane, which can be projected to the T and N components. Therefore, we use E_T and E_N, and focus on the parallel/anti-parallel propagating wave events when the local-background magnetic field is in the quasi-radial or quasi-anti-radial directions.

We regard the calibration procedure for the electric field vector (E_T, E_N) from the differential voltage data (U_X^*, U_Y^*) as a type of fitting procedure. The input conditions are known as U_X^* and U_Y^*, and the output variables are $E_T = -(\boldsymbol{V} \times \boldsymbol{B})_T$ and $E_N = -(\boldsymbol{V} \times \boldsymbol{B})_N$. The fitting parameters to be determined consist of the following parameters: (1) and (2) two offsets of the differential voltage potentials, which are caused by electronic offsets and small differences in floating potentials of the individual antenna elements (ΔU_X^* and ΔU_Y^*) (Mozer et al. 2020a); (3) effective length of the antennas (L); (4) the rotation angle θ in the X–Y plane of the spacecraft coordinates. A set of fitting equations can be obtained based on the known observables and unknown fitting parameters, and written as

$$\begin{bmatrix} \cos\theta & \sin\theta \\ \sin\theta & -\cos\theta \end{bmatrix} \begin{bmatrix} \dfrac{U_X^* + \Delta U_X^*}{L} \\ \dfrac{U_Y^* + \Delta U_Y^*}{L} \end{bmatrix} = -\begin{bmatrix} (\boldsymbol{V} \times \boldsymbol{B})_T \\ (\boldsymbol{V} \times \boldsymbol{B})_N \end{bmatrix}. \quad (1)$$

We rewrite the form of matrix operation in Equation (1) into the form of algebraic calculation:

$$\begin{aligned} &\cos\theta \cdot (U_X^* + \Delta U_X^*)/L \\ &\quad + \sin\theta \cdot (U_Y^* + \Delta U_Y^*)/L = -(V \times B)_T, \\ &\sin\theta \cdot (U_X^* + \Delta U_X^*)/L \\ &\quad - \cos\theta \cdot (U_Y^* + \Delta U_Y^*)/L = -(V \times B)_N. \end{aligned} \quad (1')$$

We rearrange the order of addition to get

$$\begin{aligned} &+U_X^* \cdot \cos\theta/L + U_Y^* \cdot \sin\theta/L + \cos\theta \cdot \Delta U_X^*/L \\ &\quad + \sin\theta \cdot \Delta U_Y^*/L = -(V \times B)_T, \\ &\quad - U_Y^* \cdot \cos\theta/L + U_X^* \cdot \sin\theta/L + \sin\theta \cdot \Delta U_X^*/L \\ &\quad - \cos\theta \cdot \Delta U_Y^*/L = -(V \times B)_N. \end{aligned} \quad (1'')$$

To employ the technique of a generalized gradient descent algorithm (GGDA; Zhang et al. 2012), we combine the fitting parameters, and rewrite Equation (1) for the time sequences with a size of M data points as

$$\begin{bmatrix} U_{X,i=1}^* & U_{Y,i=1}^* & 1/2 & 1/2 \\ \cdots & \cdots & \cdots & \cdots \\ U_{X,i=M}^* & U_{Y,i=M}^* & 1/2 & 1/2 \\ -U_{Y,i=1}^* & U_{X,i=1}^* & 1/2 & -1/2 \\ \cdots & \cdots & \cdots & \cdots \\ -U_{Y,i=M}^* & U_{X,i=M}^* & 1/2 & -1/2 \end{bmatrix} \begin{bmatrix} \dfrac{\cos\theta}{L} \\ \dfrac{\sin\theta}{L} \\ C_1 + C_2 \\ C_1 - C_2 \end{bmatrix} = -\begin{bmatrix} (\boldsymbol{V} \times \boldsymbol{B})_{T,i=1} \\ \cdots \\ (\boldsymbol{V} \times \boldsymbol{B})_{T,i=M} \\ (\boldsymbol{V} \times \boldsymbol{B})_{N,i=1} \\ \cdots \\ (\boldsymbol{V} \times \boldsymbol{B})_{N,i=M} \end{bmatrix}, \quad (2)$$

where the fitting parameters are considered as the vector on the left-hand side of Equation (2). The pair of parameters (C_1, C_2) is expressed as

$$C_1 = \frac{\cos\theta}{L}\Delta U_X^* + \frac{\sin\theta}{L}\Delta U_Y^*, \quad (3)$$

$$C_2 = \frac{\sin\theta}{L}\Delta U_X^* - \frac{\cos\theta}{L}\Delta U_Y^*. \quad (4)$$

The known variables are $U_{X,i=1\ldots M}^*$ and $U_{Y,i=1\ldots M}^*$ on the left-hand side of Equation (2), and $-(\boldsymbol{V} \times \boldsymbol{B})_{T,i\ =\ 1\ldots M}$ and $-(\boldsymbol{V} \times \boldsymbol{B})_{N,i\ =\ 1\ldots M}$ on the right-hand side of Equation (2). The unknown variables to be fitted form a vector with a size (1, 4) on the left-hand side of Equation (2), which are listed as $(\cos\theta/L, \sin\theta/L, C_1 + C_2, C_1 - C_2)^T$. These fitted parameters can be further derived to the final set of parameters (L, θ, ΔU_X^*, ΔU_Y^*). In Equation (2), there are M data points in the time sequence, using the index $i = 1,\ldots,M$, the sizes of the matrix and the vectors in Equation (2) are (4, 2 M), (1, 4), and (1, 2 M). In practice, similar to the time length adopted in (Mozer et al. 2020a), we choose a time window of 12 s as the time length to employ the fitting approach.

As the last step of the electric field calibration, we use the fitting parameters derived from the GGDA to calculate the electric field vectors based on the four-point measurements of the electric potentials at a higher time cadence of 0.0068 s. The calibrated electric field vectors are in the HGI reference frame instead of in the solar wind frame.

2.2. Formulas of Dynamic Spectra for Poynting Vector, Magnetic Helicity, and Electric Field Polarization

We adopt a method similar to that in Podesta (2009) to calculate the local-background (local-BG for short) magnetic field ($\boldsymbol{B}_{0,\text{local-BG}}$) and the local-background flow velocity

($\boldsymbol{V}_{\rm sw,local\text{-}BG}$), which are obtained through the convolution between Gaussian windows of different widths and the time sequences of the magnetic vectors and flow velocity vectors. The dynamic spectrum of the Poynting vector in the solar wind frame and its component in the R direction can be calculated as

$$\mathrm{PF}(t,p)=\frac{Re(\delta\widetilde{\boldsymbol{E}'}\times\delta\widetilde{\boldsymbol{B}}^{*})}{\mu_0} \tag{5}$$

and

$$\mathrm{PF}_R(t,p)=\frac{Re(\delta\widetilde{E'}_T\delta\widetilde{B}_N^{*}-\delta\widetilde{E'}_N\delta\widetilde{B}_T^{*})}{\mu_0}, \tag{6}$$

where the independent variables (t, p) represent the time and period, respectively. The complex variables ($\delta\boldsymbol{E}'$ and $\delta\boldsymbol{B}$) are the wavelet spectra of the electric field (in the reference frame of local-background flow) and magnetic field, respectively. The relation between the electric field spectra in the reference frame of local-background flow and its counterpart in the HGI reference frame can be expressed as

$$\delta\widetilde{\boldsymbol{E}'}=\delta\widetilde{\boldsymbol{E}}+\boldsymbol{V}_{\rm sw,local-BG}\times\delta\widetilde{\boldsymbol{B}}. \tag{7}$$

The zero-frequency part of convection electric field as contributed from the convection of the mean magnetic flux by the mean flow ($\boldsymbol{E}_0=-\boldsymbol{V}_0\times\boldsymbol{B}_0$) does not appear in the frequency-dependent Equation (7). We also note that Equation (7) is a frame transformation in the time-period domain. The local-background flow velocity of the solar wind is assumed to be a constant in the finite time-period domain to guarantee the linearity of the frame transformation. The normalized and reduced magnetic helicity is calculated according to

$$\sigma_{\rm m}(t,p)=+\frac{2Im(\delta\widetilde{B}_T\delta\widetilde{B}_N^{*})}{|\delta\widetilde{B}_T|^2+|\delta\widetilde{B}_N|^2}, \tag{8}$$

where $\delta\widetilde{B}_T$ and $\delta\widetilde{B}_N$ are the wavelet spectra of the magnetic field components B_T and B_N. Similarly, the *polarization* of the electric field about the R direction can be formulated as

$$\sigma_{E'}(t,p)=+\frac{2Im(\delta\widetilde{E'}_T\delta\widetilde{E'}_N^{*})}{|\delta\widetilde{E'}_T|^2+|\delta\widetilde{E'}_N|^2}, \tag{9}$$

where $\delta\widetilde{E}_T$ and $\delta\widetilde{E}_N$ represent the wavelet spectra of electric field components in the T and N directions, respectively.

2.3. Method of Identification and Classification of Wave Events

To identify some ideal events of kinetic waves for further detailed analysis, we propose a set of criteria and list them in Table 1. The variables PF, $\theta_{\rm RB}$, $\sigma_{\rm m}$, and $\sigma_{E'}$ represent: (1) the Poynting flux density, (2) the angle between the radial and local mean magnetic field directions, (3) the normalized reduced magnetic helicity, (4) the polarization wave electric field about the radial direction in the local mean flow frame, respectively. To make sure that the identified wave events possess the typical characteristics of kinetic wave modes, we conduct the following procedure: (1) We select a time window of 30 s to calculate an average of dynamic spectra of the variables (PF, $\theta_{\rm RB}$, $\sigma_{\rm m}$, $\sigma_{E'}$) at the timescale of 0.3 s. (2) We set the thresholds for the key variables: $\theta^{*}_{\rm RB}=30^{\circ}$, $|\sigma^{*}_{m}|=0.5$, $|\sigma^{*}_{E'}|=0.5$.

Table 1
Key Variables and Their Corresponding Criteria Used for Classification of Different Wave Modes (i.e., Fast-Magnetosonic/Whistler Mode or Alfvén-cyclotron Mode Propagating Sunward or Anti-sunward)

	Poynting Flux	$\theta_{\rm RB}$	$\sigma_{\rm m}$	$\sigma_{E'}$
Anti-sunward FWM	>0	$<\theta^{*}_{\rm RB}$ $>180\text{-}\theta^{*}_{\rm RB}$	$>+\lvert\sigma^{*}_{\rm m}\rvert$ $<-\lvert\sigma^{*}_{\rm m}\rvert$	$>+\lvert\sigma^{*}_{E'}\rvert$ $<-\lvert\sigma^{*}_{E'}\rvert$
Anti-sunward ACM	>0	$<\theta^{*}_{\rm RB}$ $>180\text{-}\theta^{*}_{\rm RB}$	$<-\lvert\sigma^{*}_{\rm m}\rvert$ $>+\lvert\sigma^{*}_{\rm m}\rvert$	$<-\lvert\sigma^{*}_{E'}\rvert$ $>+\lvert\sigma^{*}_{E'}\rvert$
Sunward FWM	<0	$<\theta^{*}_{\rm RB}$ $>180\text{-}\theta^{*}_{\rm RB}$	$<-\lvert\sigma^{*}_{\rm m}\rvert$ $>+\lvert\sigma^{*}_{\rm m}\rvert$	$<-\lvert\sigma^{*}_{E'}\rvert$ $>+\lvert\sigma^{*}_{E'}\rvert$
Sunward ACM	<0	$<\theta^{*}_{\rm RB}$ $>180\text{-}\theta^{*}_{\rm RB}$	$>+\lvert\sigma^{*}_{\rm m}\rvert$ $<-\lvert\sigma^{*}_{\rm m}\rvert$	$>+\lvert\sigma^{*}_{E'}\rvert$ $<-\lvert\sigma^{*}_{E'}\rvert$

2.4. Estimating the Real and Imaginary Frequencies of Wave Activity

Based on a Fourier transform of the Faraday equation, we obtain

$$\frac{\omega+i\gamma}{k}\delta\widetilde{\boldsymbol{B}}=\hat{\boldsymbol{e}}_k\times\delta\widetilde{\boldsymbol{E}'}, \tag{10}$$

where ω and γ represent the real and imaginary parts of the wave frequency, k and $\hat{\boldsymbol{e}}_k$ are the wavenumber and unit wavevector, respectively. If the wave is a transverse wave with both electric and magnetic field fluctuations oscillating in the directions perpendicular to the wavevector, as it is the case in quasi-parallel propagating Alfvén/ion-cyclotron waves and fast-magnetosonic/whistler waves for example, Equation (10) can be rewritten as

$$\frac{\omega_r+i\gamma}{k}=\frac{\delta\widetilde{\boldsymbol{E}'}\times\delta\widetilde{\boldsymbol{B}}^{*}}{\delta\widetilde{\boldsymbol{B}}\cdot\delta\widetilde{\boldsymbol{B}}^{*}}\cdot\hat{\boldsymbol{e}}_k. \tag{11}$$

Therefore, based on the wavelet spectra of the electric and magnetic field, we obtain the dynamic spectra of the dispersion relation and growth rate

$$\begin{pmatrix}\frac{\omega}{k}\\ \frac{\gamma}{k}\end{pmatrix}=\begin{pmatrix}Re\left(\frac{\delta\widetilde{\boldsymbol{E}'}\times\delta\widetilde{\boldsymbol{B}}^{*}}{\delta\widetilde{\boldsymbol{B}}\cdot\delta\widetilde{\boldsymbol{B}}^{*}}\right)\\ Im\left(\frac{\delta\widetilde{\boldsymbol{E}'}\times\delta\widetilde{\boldsymbol{B}}^{*}}{\delta\widetilde{\boldsymbol{B}}\cdot\delta\widetilde{\boldsymbol{B}}^{*}}\right)\end{pmatrix}\cdot\hat{\boldsymbol{e}}_k. \tag{12}$$

We note that the above equation is a simplified version for the situation of quasi-parallel transverse waves. In general, the wave group speed is determined by the ratio of energy-flux density to the energy density, with the energy-flux density being the sum of the Poynting flux and kinetic flux and the energy density being contributed by the fluctuating electromagnetic field energy and plasma kinetic energy (Stix 1992; Swanson 2003). According to the Doppler-shift effect caused by the solar wind flow, the relation between wave frequencies ($\omega_{\rm sc}$) in the spacecraft reference frame and in the solar wind flow reference frame ($\omega_{\rm pl}$) can be expressed as

$$\frac{\omega_{\rm sc}}{k}=\frac{\omega_{\rm pl}}{k}+V_{\rm sw}\cos\theta_{kV}, \tag{13}$$

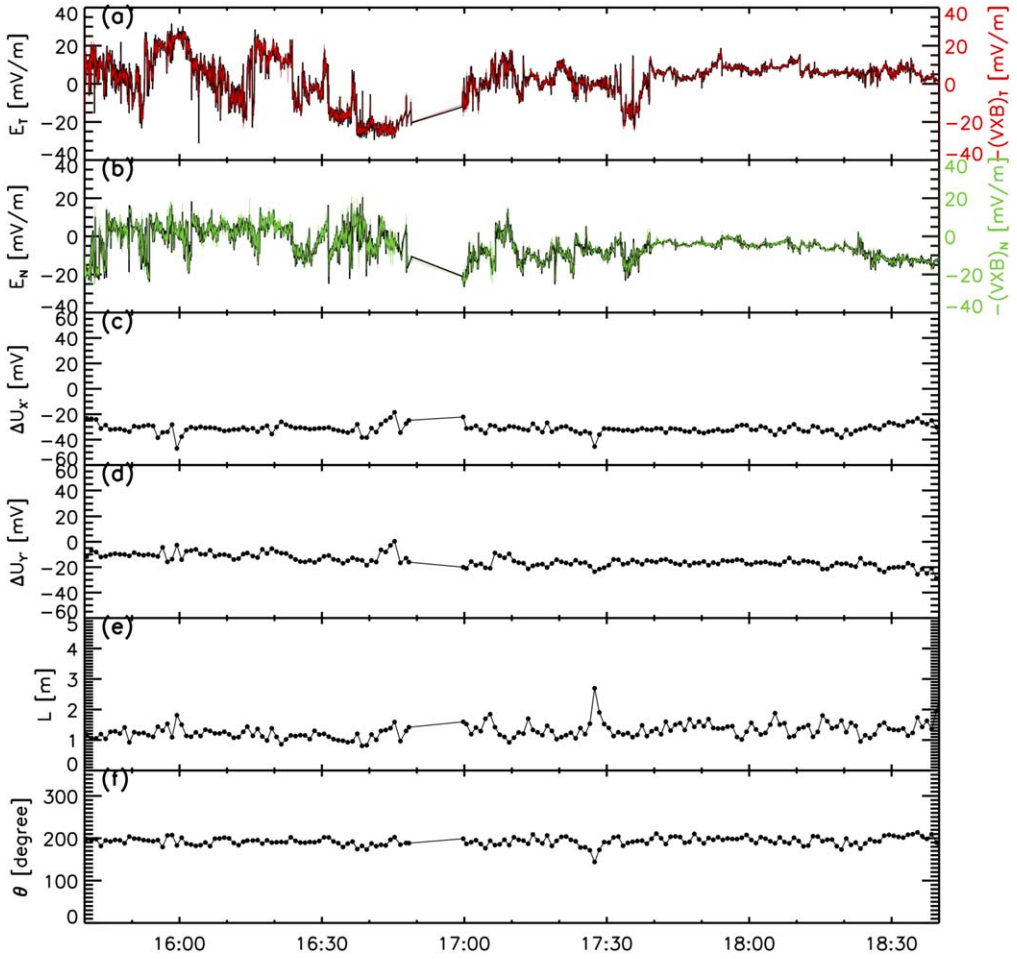

Figure 1. Electric-field calibration result in the time interval of [15:40, 18:40] UT on 2018 November 4. (a) Time sequences of the electric field component E_T obtained from calibration (black) and the inductive electric field component $-(V \times B)_T$ (red). (b) Time sequences of the electric field component E_N obtained from calibration (black) and the inductive electric field component $-(V \times B)_N$ (green). (c)–(f) Time sequences of the fitting parameters: ΔU_X^*, ΔU_Y^*, L, and θ.

where $V_{\rm sw}$ is the local-background solar wind flow velocity, and θ_{kV} is the angle between $V_{\rm sw}$ and the wavevector $\boldsymbol{k}$. Equation (13) describes the Doppler-shift effect on the plasma wave frequency due to advection by the solar wind flow relative to the spacecraft as an observer. It can be simplified to Taylor's hypothesis as $\omega_{\rm sc} \sim kV_{\rm sw}\cos\theta_{kV}$, when the flow speed is much greater than the wave propagation speed ($V_{\rm sw} \gg V_{\rm A}$). However, this assumption is not always satisfied in the case with PSP. The direction of the wavevector can be determined without the problem of 180° ambiguity by considering the analysis result from the *singular value decomposition* (SVD) method and the direction of the Poynting vector relative to the background magnetic field. For convenience, hereafter, we drop the subscript "pl" in "$\omega_{\rm pl}$" for simplicity. Based on Equations (12) and (13), we further derive formulas of k, ω, and γ, which read as

$$k = \omega_{\rm sc}\frac{1}{\omega/k + V_{\rm sw}\cos\theta_{kV}}, \tag{14}$$

$$\omega = \omega_{\rm sc}\frac{\omega/k}{\omega/k + V_{\rm sw}\cos\theta_{kV}}, \tag{15}$$

$$\gamma = \omega_{\rm sc}\frac{\gamma/k}{\omega/k + V_{\rm sw}\cos\theta_{kV}}. \tag{16}$$

We carry out the following derivations to arrive at Equations (14)–(16). First, we re-express the denominator on the left-hand side of Equation (13) as the quotient of the numerator on the left divided by the right, thereby arriving at Equation (14). Then, we multiply both sides of Equation (14) by the first and second lines of Equation (12) to obtain Equations (15) and (16), respectively.

To validate the credibility of applying Equation (6) to the measurement of the Poynting vector, we also propose a formula for calculating the phase difference between the wave electric field $\delta\boldsymbol{E}'$ ($\phi(\delta\boldsymbol{E}')$) and the wave magnetic field $\delta\boldsymbol{B}$ ($\phi(\delta\boldsymbol{B})$) (see Equation (17)), and calculate its distribution in the time and scale dimensions. The phase difference may be written as

$$\phi(\delta\boldsymbol{B}_\perp, \delta\boldsymbol{E}'_\perp) = \phi(\delta\boldsymbol{B}_\perp) - \phi(\delta\boldsymbol{E}'_\perp), \tag{17}$$

where both $\delta\boldsymbol{B}_\perp$ and $\delta\boldsymbol{E}'_\perp$ correspond to the wavelet decomposition of the original time sequences at the same scales. The available timescale range for the phase difference is determined by the common range of the timescale ranges for the two variables $\boldsymbol{B}_\perp$ and $\boldsymbol{E}'_\perp$. The polarity of the Poynting vector can be inferred from the phase difference: (1) $\delta\boldsymbol{E}' \times \delta\boldsymbol{B}$ is positive for $\phi(\delta\boldsymbol{B}_\perp, \delta\boldsymbol{E}'_\perp) \in (0, 180)°$; (2) $\delta\boldsymbol{E}' \times \delta\boldsymbol{B}$ is negative for $\phi(\delta\boldsymbol{B}_\perp, \delta\boldsymbol{E}'_\perp) \in (-180, 0)°$.

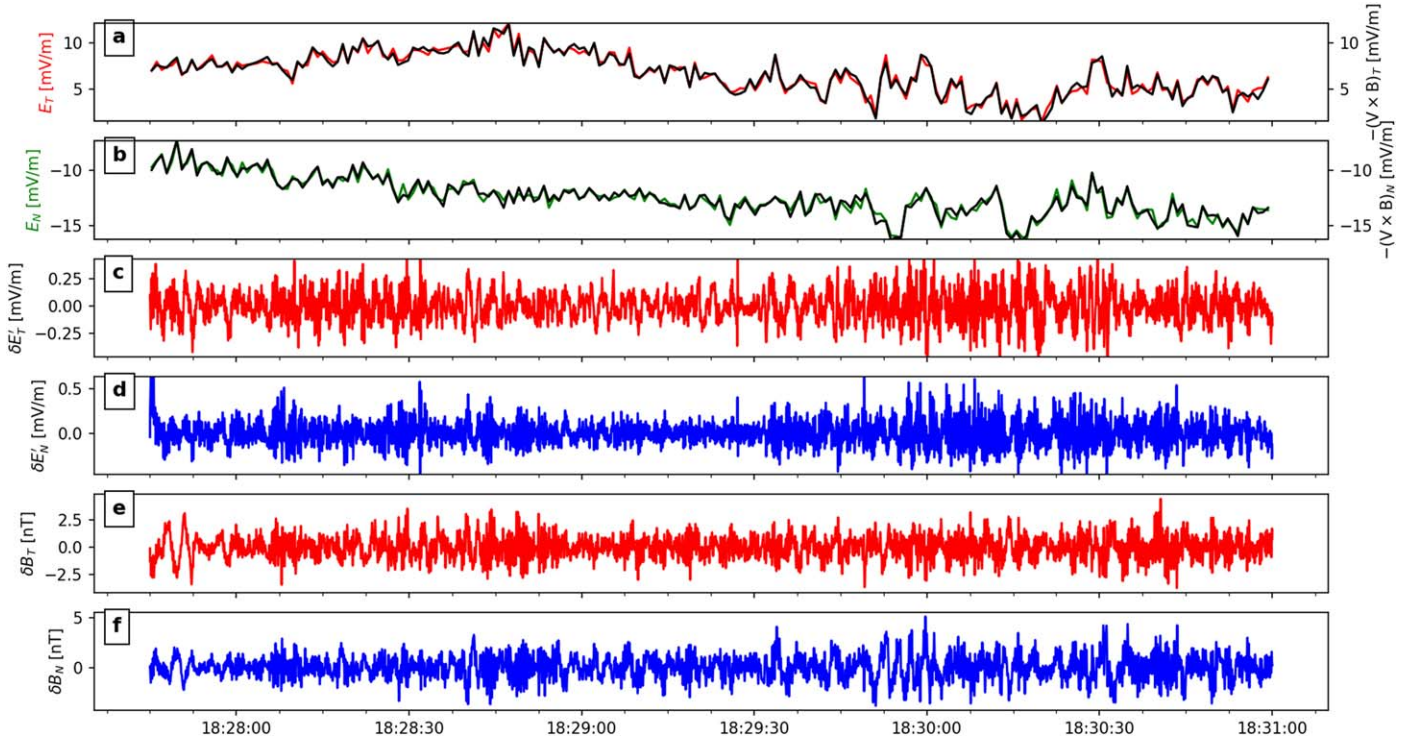

Figure 2. Time sequences of the electric and magnetic field for a wave event in the solar wind measured by PSP during its first encounter. (a) Consistency between the calibrated E_T from four-point electric potential differences (red) and the calculated E_T from $-\boldsymbol{V} \times \boldsymbol{B}$ (black). (b) Good match between the calibrated E_N (green) and the calculated E_N (black). (c) and (d) The bandpass ($f_{SC} \in [0.2, 10]$ Hz) wave fluctuations of the E_T and E_N components in the local solar wind background flow frame ($\delta E'_T$ and $\delta E'_N$). (e) and (f) The bandpass ($f_{SC} \in [0.2, 10]$ Hz) wave fluctuations of the B_T and B_N components.

3. Event Analysis

3.1. Analysis Steps

We conduct the search and analysis of interesting wave events based on the measurements from PSP during its first encounter on 2018 November 4. We break down this task into six steps. (1) The first step is to calibrate the electric field segment by segment according to Equation (2), and thereby realizing the conversion from the four-point electric potentials to the 2D electric field vectors. (2) We then invoke Equation (7) to realize the coordinate transformation of the electric field from the spacecraft reference frame to the reference frame of the local solar wind background flow. (3) We calculate the dynamic spectrum of the Poynting flux along the R direction according to Equation (6). (4) We calculate the dynamic spectrum of the magnetic helicity and electric polarization about the R direction with Equations (8) and (9), respectively. (5) We calculate ω/k and γ/k for the wave events. (6) We estimate the wavenumber, real part, and imaginary part of wave frequency according to Equations (14)–(16). We classify the wave events based on the analysis results of the above first five steps and as per Table 1. In this way, we accomplish the goal of diagnosing the key characteristics (e.g., propagation direction, the polarization, and the growth/damping rate) of the wave events.

3.2. Power Spectral Densities and Polarization of Wave Electromagnetic Fields

In Figures 1(a) and (b), the calibrated electric fields are consistent with the inductive electric fields. During the interval from 15:40–18:40 UT on 2018 November 4, the four fitting parameters (ΔU_X^*, ΔU_Y^*, L, θ) remain at a relatively stable level except for a few occasional jumps (Figures 1(c)–(f)). For example, ΔU_x^* has a mean of -31.5 mV and a standard deviation of 3.5 mV, δU_Y^* has a mean of -15.5 mV and a standard deviation of 4.6 mV, L has a mean of 1.26 m and a standard deviation of 0.25 m, θ has a mean of 193.°8 and a standard deviation of 9.°5. In addition, consistent with the research results of Mozer et al. (2020a) on the measurement of DC and low-frequency electric fields, the equivalent antenna length used for calibrating low-frequency electric fields is appropriate, which is within the range of 1–2 m. We also note from Mozer et al. (2020a) that when the frequency in the spacecraft reference frame increases, the equivalent length of the antenna will also increase, and finally approach the geometric length of the antenna when the frequency exceeds 20 Hz.

As a typical example, we show a wave event of outward propagation, right-hand polarization about $\boldsymbol{B}_0$, and positive growth. The time interval of this event is between [18:28, 18:31] UT on 2018 November 4. In Figures 2(a) and (b), we display and compare the calibrated electric field (E_T, E_N) and the induced electric field based on the measurements of magnetic field and bulk velocity ($-(\boldsymbol{V} \times \boldsymbol{B})_T$, $-(\boldsymbol{V} \times \boldsymbol{B})_N$). The two types of electric field match well with one another. Therefore, we use the calibrated electric field to analyze the propagation direction and growth/damping rate of the observed wave. We apply wavelet decomposition to the time sequences of the electric and magnetic field components (E_T, E_N, B_T, B_N), and obtain the corresponding bandpass waves in the frequency range of [0.2, 10] Hz, which are illustrated in Figures 2(c)–(f), respectively. To further diagnose how the wave propagates in the solar wind reference frame, we transform the electric field from the spacecraft reference frame to the solar wind reference

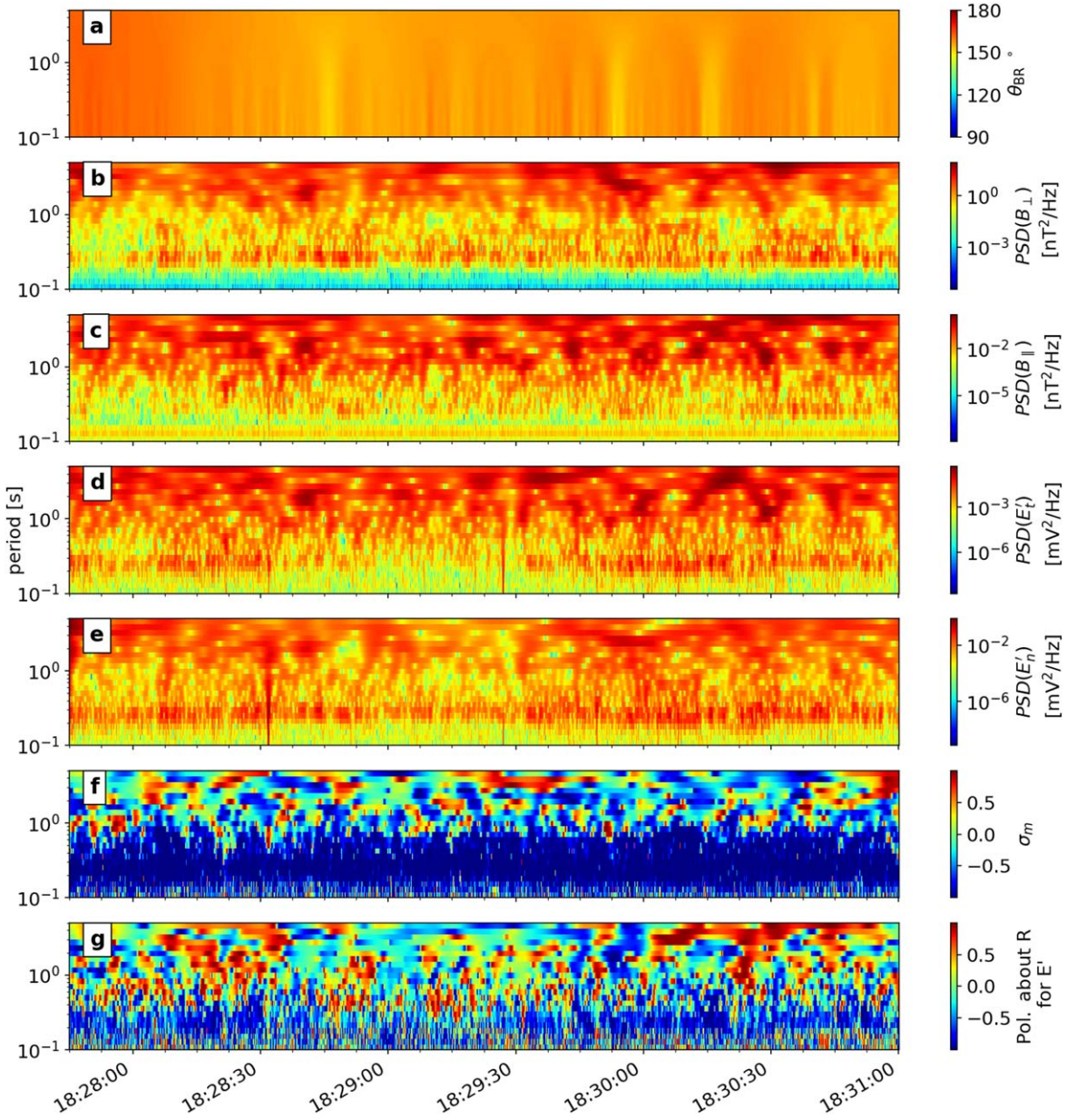

Figure 3. Dynamic spectra of the magnetic and electric fields. (a) Time-period distribution of $\theta_{\rm BR}$, the angle between the local-background magnetic field direction and the radial direction. (b) and (c) Time-period distribution of power spectral densities of transverse and longitudinal magnetic field components (PSD($\delta B_\perp$) and PSD ($\delta B_\parallel$)). (d) and (e) Time-period distribution of PSD($\delta E'_T$) and PSD($\delta E'_N$) in the local solar wind background frame. (f) Time-period distribution of $\sigma_{\rm m}$. (g) Time-period distribution of the electric field polarization about the R direction.

frame. Within the time interval of 10 minutes containing the wave event, the relative fluctuations of number density ($\delta N/N_0$) and magnetic field strength ($\delta|B|/|B|_0$) are very weak ($\delta N/N_0 \sim 0.03$ and $\delta|B|/|B|_0 \sim 0.01$), confirming that the ambient solar wind plasma can be approximated as homogeneous.

We conduct a detailed analysis of the magnetic field (including the local-background and the fluctuating magnetic field) and the electric field (the fluctuating electric field in the local solar wind background frame). We find that the local-background magnetic field direction is mainly sunward with $\theta_{BR} \gtrsim 140°$ (see Figure 3(a)). The magnetic field fluctuations are mainly in the transverse directions, indicating the state of approximate incompressibility (PSD($\delta B_\perp$) in Figure 3(b) is dominant over PSD($\delta B_\parallel$) in Figure 3(c)). For most times of the interval, there are evident enhanced signals of PSD($\delta B_\perp$) at periods of [0.2, 0.4] s (see Figure 3(b)). Since $B_{0,\rm local}$ is quasi-anti-parallel to the R direction, the T and N directions can be approximated as the two directions perpendicular to $B_{0,\rm local}$, rendering convenience for the analysis of the transverse wave electric field. We point out the existence of wave signals in the period range of [0.2, 0.4] s, as indicated by the enhanced signals of PSD($\delta E'_t$) and PSD($\delta E'_n$) in Figures 3(d) and (e), respectively. The magnetic helicity spectrum as calculated according to Equation (8) shows negative polarity in the period range of [0.2, 0.4] s (see Figure 3(f)). Likewise, the polarization of the wave electric field (in the local solar wind background frame) around the R direction, which is calculated from Equation (9), appears with negative polarity (Figure 3(g)). The good match between magnetic helicity and electric polarization

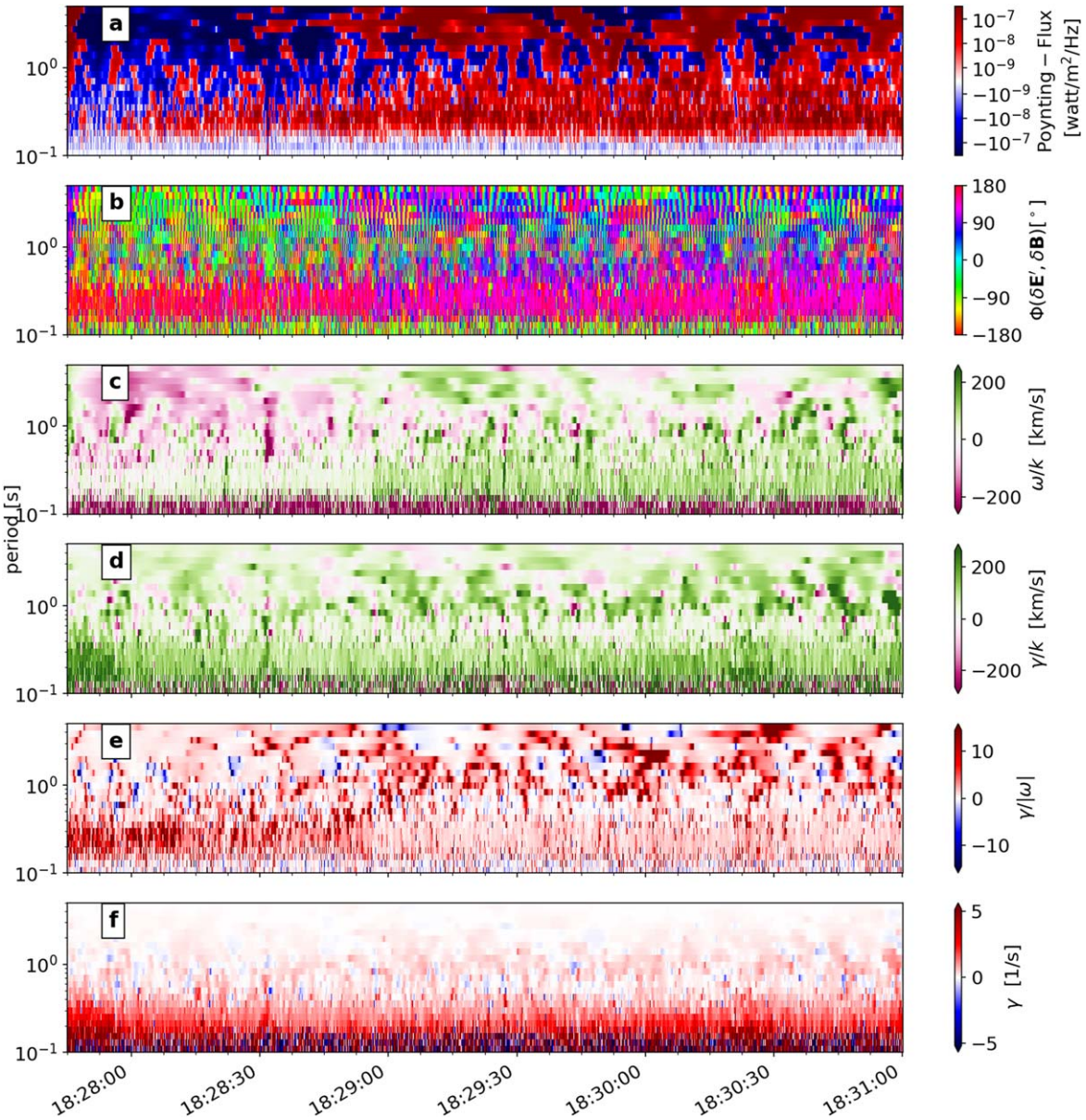

Figure 4. Analysis result of wave propagation and growth/damping. (a) Time-period distribution (dynamic spectrum) of the Poynting flux density component PF_R. (b) Time-period distribution of $\phi(\delta E'_\perp, \delta B_\perp)$ $(=\phi(\delta B_\perp) - \phi(\delta E'_\perp))$. (c) Dynamic spectra of ω/k. (d) Dynamic spectra of γ/k. (e) Dynamic spectra of $\gamma/|\omega|$. (f) Dynamic spectra of γ.

indicates the high-quality measurements of the electric and magnetic fields of this wave event, which can be further analyzed to investigate its propagation direction and activity of growth/dissipation. An identification and analysis of the wave events on the same day (2018 November 4) has been conducted by Mozer et al. (2020a) and Bowen et al. (2020a). The main difference of analysis between their analysis and ours lies in the different reference frames used for the electric field. We adopt the local-background flow reference frame instead of the spacecraft reference frame. We have verified the identification method proposed in this work by applying it to the cases reported by Bowen et al. (2020a). We are aware that the spacecraft reaction wheels introduced a very narrow band of coherent noise between 8 and 8.5 Hz. The wave signal analyzed in this work is located around [3, 6] Hz, different from that caused by the reaction wheels. Following the process presented by Bowen et al. (2020c), we adopt a narrow-band notch filter to attenuate the power at the frequency corresponding to the reaction wheel effect before further wavelet analysis.

4. Diagnosis of Propagation and Evolution of Wave Events

According to Equation (6), we calculate and illustrate the dynamic spectrum of the Poynting flux density in the R direction (PF_R) (see Figure 4(a)). During the time interval of [18:27:45, 18:31:00] and in the period range of [0.1, 0.5] s, PF_R is greater than 0, suggesting that the waves propagate outward quasi-anti-parallel to the sunward local-background magnetic field direction. Referring to Table 1, we identify this wave event as outward propagating fast-magnetosonic/whistler waves with right-hand polarization of electromagnetic field vectors about the background magnetic field direction. In Figure 4(b), we observe that the phase angle differences,

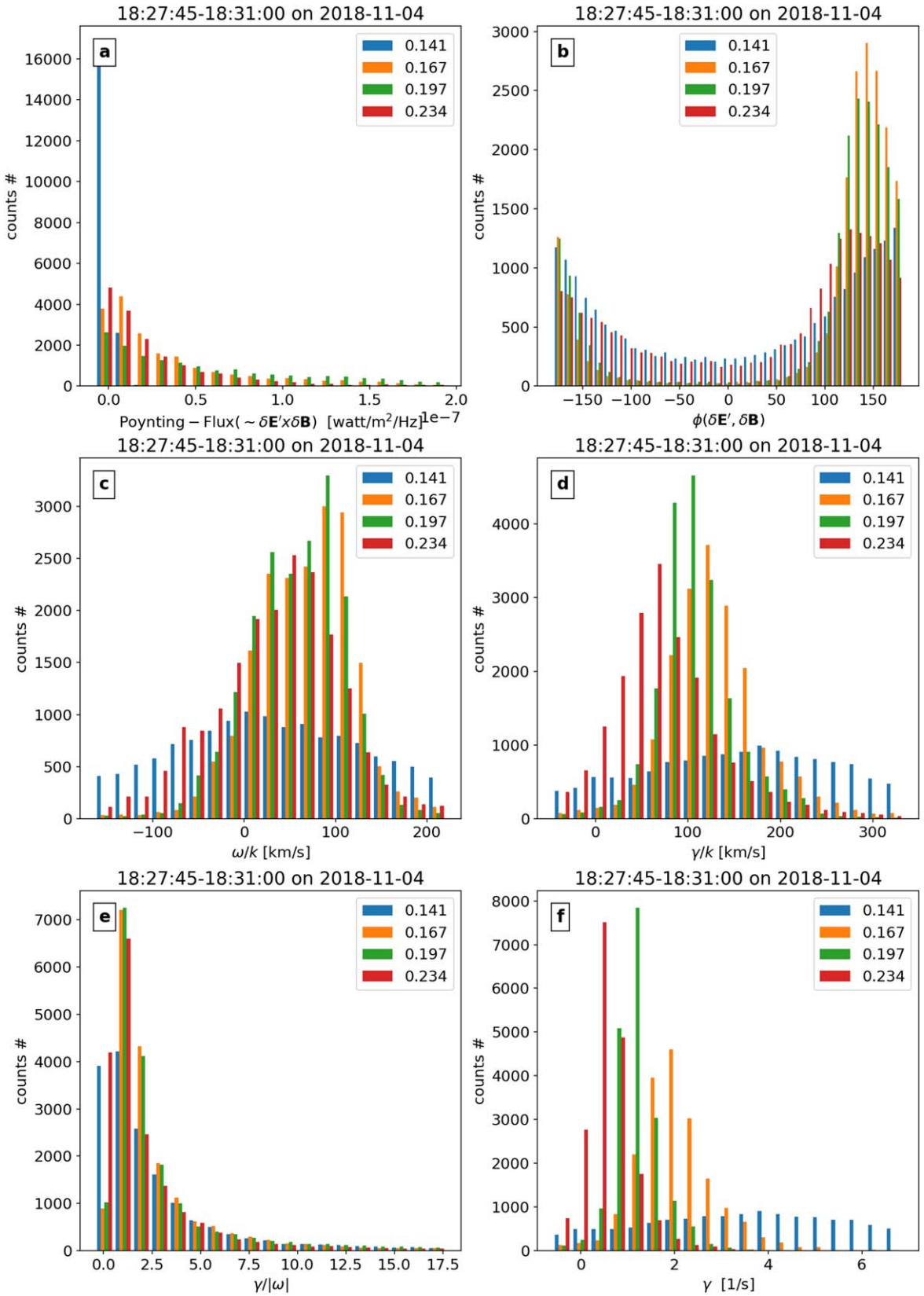

Figure 5. Occurrence frequency distribution (i.e., un-normalized probability distribution function) of multiple variables related with wave propagation and evolution at seven different timescales ($\tau = 0.141$, 0.167, 0.197, 0.234, 0.277, 0.329, 0.390 s). (a) Frequency histogram of PF_R component. (b) Frequency histogram of $\phi(\delta E'_{\perp}, \delta B_{\perp})$. (c) Frequency histogram of ω/k. (d) Frequency histogram of γ/k. (e) Frequency histogram of $\gamma/|\omega|$. (f) Frequency histogram of γ.

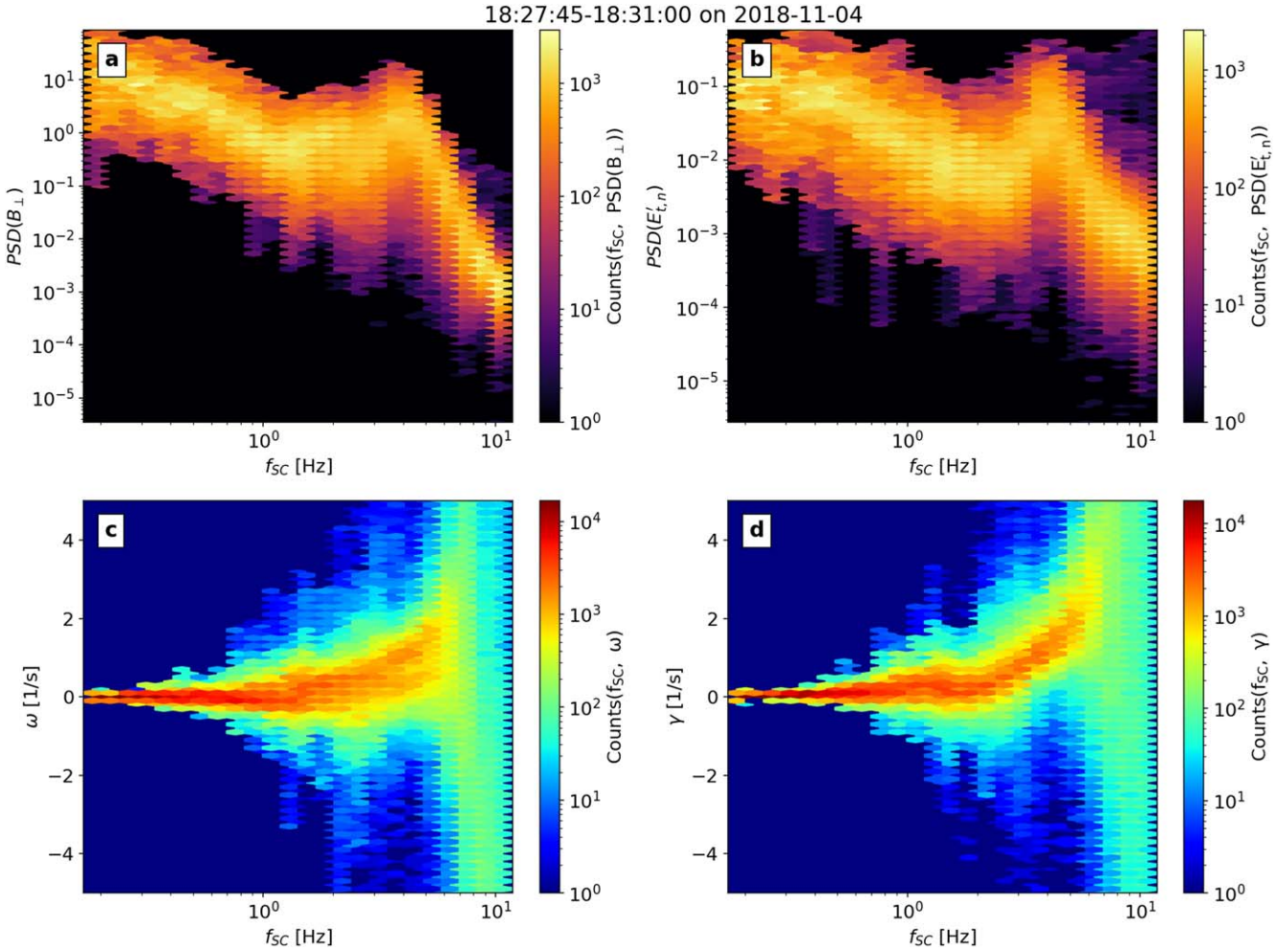

Figure 6. Evidence of fast-magnetosonic/whistler wave growth leading to amplitude enhancement. (a) and (b) Occurrence frequency distribution of PSD($\delta B_\perp$) and PSD($\delta E'_{T,N}$) at various frequencies in the spacecraft frame. (c) and (d) Occurrence frequency distribution of ω and γ at various frequencies in the spacecraft frame.

$\phi(\delta \boldsymbol{B}_\perp, \delta \boldsymbol{E}'_\perp) \in (0, 180)^\circ$ and $\phi(\delta \boldsymbol{B}_\perp, \delta \boldsymbol{E}'_\perp) \in (-180, 0)^\circ$ correspond to $\mathrm{PF}_R > 0$ and $\mathrm{PF}_R < 0$ in Figure 4(a), respectively.

We calculate the dynamic spectra of ω/k and γ/k according to Equation (12) (see Figure 4(c), (d)). Moreover, we calculate the dynamic spectral distribution of $\gamma/|\omega|$ and γ according to Equation (16) (see Figure 4(e), (f)). In the case of our study, we approximate θ_{kV} in Equation (16) with 0° since $\theta_{kB} \sim 180^\circ$ and $\theta_{BV} \sim 180^\circ$ during the interval of study. We can see that γ is most of the time greater than 0 in the time-period distribution, especially in the period range of [0.1, 0.5] s. The percentages of time intervals with positive Poynting flux ($\mathrm{PF}_R > 0$ corresponds to anti-sunward propagation) and positive γ ($\gamma > 0$ represents wave growth) are about 72% and 90% at the timescales of interest (i.e., from 0.1–0.5 s). This evidence strongly suggests that the observed fast-magnetosonic/whistler waves are outward propagating and growing during the time of observation.

We apply a further statistical analysis of the above results of wave propagation and growth. We select four timescales ($\tau = 0.141$, 0.167, 0.197, 0.234 s), and count the value-dependent occurrence frequency distribution of multiple variables (e.g., PF_R, $\phi(\delta E'_\perp, \delta B_\perp)$, ω/k, γ/k, $\gamma/|\omega|$, γ) (see Figures 5(a)–(f)). The four timescales out of the 24 timescales between 0.1 and 0.5 s are chosen for wavelet transformation according to Equations (9) and (10) in Torrence & Compo (1998), and correspond to the timescales with a clear wave signal. At scales shorter than 0.5 s, PF_R appears more on the positive side, $\phi(\delta E'_\perp, \delta B_\perp)$ appears more (about 68%) in the angle range of (0, 180)°. The distribution of γ is asymmetric, with more intervals on the side greater than 0, indicating the nature of local excitation and emission for the studied fast-magnetosonic/whistler waves.

To view the variation of PSD($\delta B_\perp$), PSD($\delta E'_{T,N}$), ω and γ as a function of f_{sc} from a statistical perspective, we plot the occurrence frequency distribution in the 2D space of (f_{sc}, PSD($\delta B_\perp$)), (f_{sc}, PSD($\delta E'_{T,N}$)), (f_{sc}, ω), and (f_{sc}, γ) (see Figure 6). We can see from Figures 6(a) and (b) that, both PSD($\delta B_\perp$) and PSD($\delta E'_{T,N}$) show an obvious spectral bump around $f_{sc} \sim 4.0$ Hz. The noise caused by the reaction wheels is constrained in a narrow band between [8.0, 8.5] Hz, which is outside the spectral bump reported here. Such spectral bump structure indicates that, the wave signal is stronger than the background turbulence level, probably due to its excitation and unstable growth. Unlike for damped or freely propagating waves, the growth rate (γ) of the active wave evidently exceeds the zero level (see Figure 6(d)), and even approaches a level comparable to the derived wave frequency (Figure 6(c)), offering further direct evidence that the active wave is growing during the time of the observation. At higher frequency beyond the PSD's bump, the occurrence frequency distributions of both ω and γ become diffusive (see the right end of Figures 6(c) and (d)), probably due

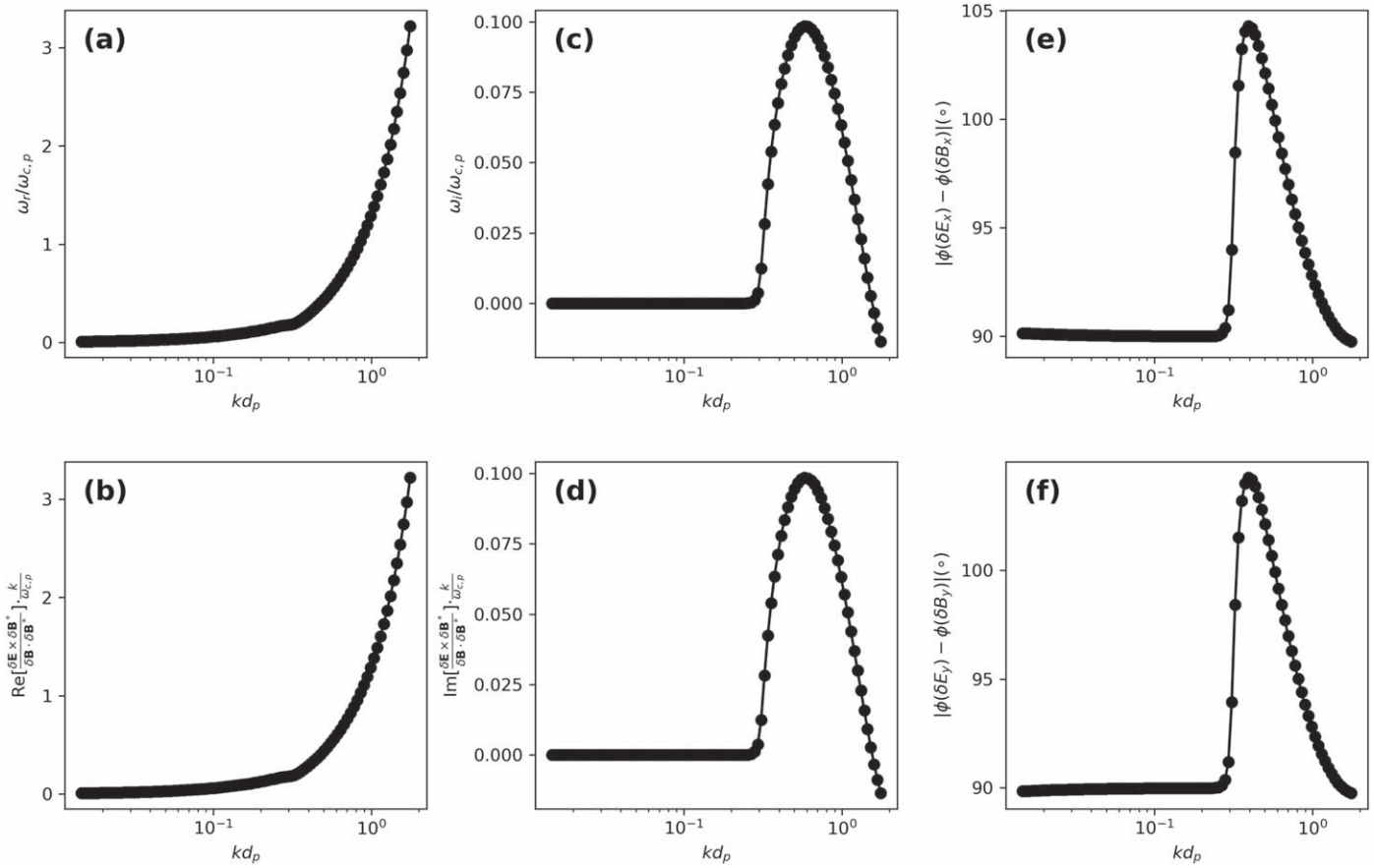

Figure 7. (a) and (c) Normalized real part (a) and imaginary part (c) of wave frequency as a function of the normalized wavenumber for the fast-magnetosonic/whistler wave branch, which is obtained from PKUES code package according to the linear plasma theory. (b) and (d) Real part (b) and imaginary part (d) of the formula involving the information of complexed Poynting flux density and magnetic energy density, which are in another form of Equation (12) proposed in this work. Through comparison, one can trust the reliability of adopting Equation (12) to estimate the dispersion relation and growth/damping rate spectrum. (e) and (f) Phase differences between the electric fields and magnetic fields, the part greater than 90° indicate that the wave is growing with a positive imaginary part of wave frequency.

to the uncertainty of the electric field measurements at higher frequency.

To corroborate our technique for the derivation of the spectra of dispersion relation and growth rate, we provide a benchmark test of our method. In the benchmark test, we carry out the following five analysis steps. (1) We set a plasma condition conforming to the solar wind situation in the inner heliosphere (e.g., a bi-Maxwellian distribution consisting of proton core and beam populations with a relative drift of the order the local Alfvén speed between each other). Then, according to linear plasma theory, we determine the unstable eigenmodes of plasma waves by invoking the codes of Plasma Dispersion Relation Kinetics (PDRK) and Plasma Kinetics Unified Eigenmode Solutions (PKUES; Xie & Xiao 2016; Luo et al. 2022). (2) We compare the spectra of the dispersion relation and growth/damping rate between the direct result from linear plasma theory with the PKUES code and the result from Equation (12) to the eigenmode electromagnetic field fluctuations ($\delta \boldsymbol{E}'$ and $\delta \boldsymbol{B}$). We find consistency between the two results (see Figure 7). (3) We set a power spectral profile (with a power law plus a bulge) of the magnetic field fluctuations, and obtain the associated electric field power spectral densities. (4) We produce the sampling sequences of the electromagnetic field fluctuations, which are modeled according to the power spectra and phase spectra of the electromagnetic fields. (5) We apply our analysis method to the virtually sampled sequences of the electromagnetic field fluctuations. As a result, we obtain the information about the power spectral densities, the dispersion relation, and the growth rate spectrum, which are denoted by the histogram distributions in (k, PSD($B_\perp$), (k, PSD($E'_\perp$), (k, ω), and (k, γ) (see Figure 8). We demonstrate that our approach is able to determine the dispersion relation and growth rate spectrum of the preset fast-magnetosonic/whistler wave. At the high-frequency end, the γ spectrum shows a diffuse distribution, which may be related to the aliasing effect at high frequencies.

5. Discussion and Conclusions

In this work, we propose a method to quantify the energy-flux density of wave propagation (i.e., Poynting flux density for electromagnetic waves) and the growth/dissipation rate spectrum. Based on this method, we further put forward a set of diagnosis criteria for the nature of kinetic wave events in the heliosphere. We apply this analysis method and the diagnosis criteria to in situ measurements from PSP in the inner heliosphere. As an example, we identify an event of outward propagating fast-magnetosonic/whistler waves with right-hand polarization. For this wave event, we provide the dynamic spectra of physical variables (power spectral densities, magnetic helicity, electric field polarization, Poynting flux density, phase difference between electric and magnetic fields, wave frequency, and normalized rate of change of the wave energy density). We find that the wave event is not in a time steady

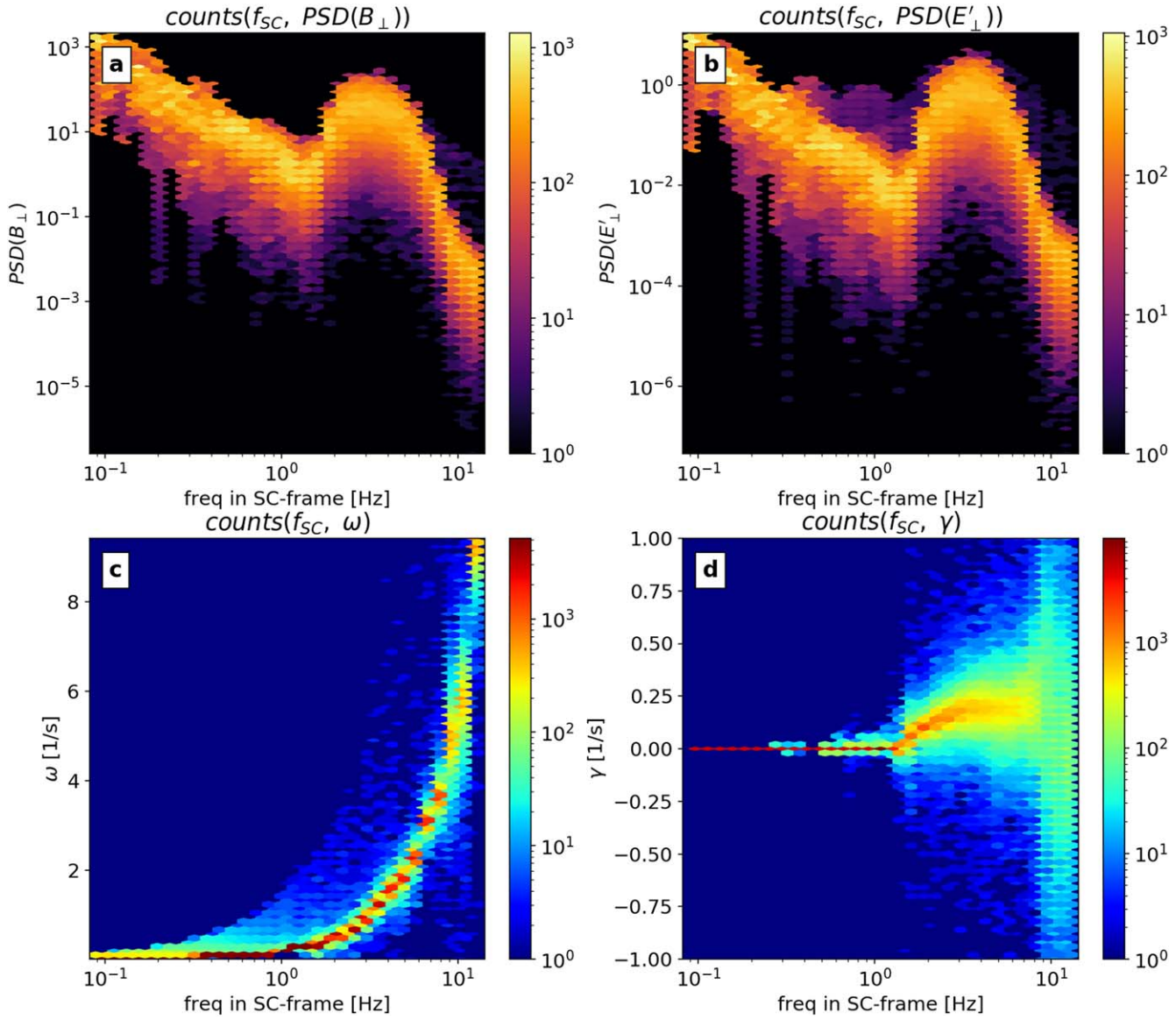

Figure 8. Analysis results of applying the diagnosis technique to the time sequences of synthetic electromagnetic field fluctuations of fast-magnetosonic/whistler wave branch, which is sampled by a virtual spacecraft along the parallel direction. (a) Statistical distribution of the transverse magnetic power spectral density vs. the frequency in the virtual spacecraft reference frame. (b) Similar to (a) but for the transverse electric field fluctuations. (c) and (d) Statistical distribution of the real part (c) and imaginary part (d) of the wave frequency as obtained from Equations (15) and (16).

state but in the temporally growing phase, evidenced by the positive bump of the $\gamma(f_{sc})$ spectral profile, which is physically responsible for the spectral bumps appearing on the PSDs of the electric and magnetic field fluctuations.

We do not require that the approximation of the electric field at MHD scales with the inductive electric field is applicable to the electric fields at much smaller, kinetic scales. We employ the fitting parameters to the differential voltage data at slightly higher frequency to obtain the calibrated electric field data. The frequency we studied is not particularly high, below 10 Hz. Under Taylor's hypothesis, the wave signal of the spectral bump has a wavenumber of $kd_i \sim 1$ and $k\rho_i \sim 0.53$ in units of the ion inertial length (d_i) and ion thermal gyroradius (ρ_i). If the contribution of the plasma wave frequency is taken into account, then kd_i and $k\rho_i$ of the spectral peak could be smaller and the corresponding wavelength could be larger. Therefore, the spatial scale of the wave signal is still close to the MHD scales. On the other hand, the time cadence of the ion fluid velocity used to calibrate the electric field is relatively high (about 1.7 Hz), which also facilitates the calibration of the electric field below 10 Hz.

According to Malaspina et al. (2016), the preamplifier gain is very flat and the phase correction is small for the differential voltage data at low frequencies (below ~100 kHz). Therefore, in the Level-2 differential voltage data, the preamplifier gain is set to unity and the preamplifier phase correction is not required. Moreover, digital filter effects, which can be deterministic, have been corrected for the Level-2 data. The effect of the plasma sheath surrounding the spacecraft on the differential voltage data is more complicated and investigated by Mozer et al. (2020a). We adopt a technique similar to that of Mozer et al. (2020a) to take the plasma sheath effect into account. The complex transfer function associated with the fluxgate magnetometers (MAGs) can be expressed with a single-pole Butterworth filter (Bowen et al. 2020b). The gain of the low-pass filter has almost no attenuation below 10 Hz (the absolute value of the transfer function is greater

than 0.99), and the phase shift is very small (less than 5°) below 10 Hz. Moreover, when we compare the Level-2 MAG data and the Level-3 merged *SCaM* data, which combines the measurements from SC and MAG, we find that the two levels of data in the magnetic field signal with periods greater than 0.1 s are almost the same. Therefore, the response functions of the electromagnetic field measurements do not affect our analysis at ion kinetic scales.

This work addresses the issue of the origin of kinetic waves in the inner heliosphere. The frequency of the observed kinetic waves in the spacecraft reference frame is around $3.3f_p$ where $f_p \sim 1.2$ Hz is the proton gyrofrequency. We point out that kinetic waves are not necessarily created in the solar wind source region, though some proportion of waves may be launched from the solar atmosphere through magnetic reconnection or turbulent advection shaking (Zank et al. 2020; He et al. 2021). Instead they can be locally excited and grow due to instability in the inner heliosphere. The results of this work indicate that the inner heliosphere shall be regarded as a critical region for the birth and development of kinetic waves. This suggests that the inner heliosphere exhibits complex wave-particle coupling processes, involving the velocity distributions of various plasma species and the time-varying evolution of different wave modes. The free energy responsible for the fast-magnetosonic/whistler waves may come from the drift ion population, electron heat flux, and electron thermal anisotropy (Verscharen et al. 2013; Narita et al. 2016; Stansby et al. 2016; Tong et al. 2019; Sun et al. 2020). In the future, we require a combination of both the electromagnetic field information and the particle phase space density to explore the mystery of kinetic waves and their wave-particle interactions in the inner heliosphere in a comprehensive way.

We thank the NASA Parker Solar Probe Mission and the FIELDS and SWEAP teams for use of data. PSP data is available on SPDF (https://cdaweb.sci.gsfc.nasa.gov/index.html/). The work at Peking University is supported by NSFC under contract Nos. 42174194 and 41874200, and by CNSA under contract Nos. D020301, D020302, and D050601, as well as National Key R&D Program of China No. 2021YFA0718600. D.V. from UCL is supported by the STFC Ernest Rutherford Fellowship 354 ST/P003826/1 and STFC Consolidated grant ST/S000240/1. G-Q. Z. is supported by the NSFC under contract No. 41874204 and partly by the Project for Scientific Innovation Talent in Universities of Henan Province (19HASTIT020). We are grateful to F. Mozer, T. Bowen, and M. Pulupa from the FIELDS instrument team for their kind help in explaining the FIELDS measurements and calibration.

ORCID iDs

Jiansen He https://orcid.org/0000-0001-8179-417X
Ying Wang https://orcid.org/0000-0001-8245-9752
Xingyu Zhu https://orcid.org/0000-0002-1541-6397
Die Duan https://orcid.org/0000-0002-6300-6800
Daniel Verscharen https://orcid.org/0000-0002-0497-1096
Guoqing Zhao https://orcid.org/0000-0002-1831-1451

References

Bale, S., Goetz, K., Harvey, P., et al. 2016, SSRv, 204, 49
Bale, S., Kellogg, P., Mozer, F., Horbury, T., & Reme, H. 2005, PhRvL, 94, 215002
Boardsen, S., Jian, L., Raines, J., et al. 2015, JGRA, 120, 10
Bowen, T. A., Bale, S. D., Bonnell, J., et al. 2020a, ApJ, 899, 74
Bowen, T. A., Bale, S. D., Bonnell, J. W., et al. 2020b, JGRA, 125, e27813
Bowen, T. A., Mallet, A., Huang, J., et al. 2020c, ApJS, 246, 66
Chandran, B. D., & Perez, J. C. 2019, JPlPh, 85, 905850409
Chen, C., Boldyrev, S., Xia, Q., & Perez, J. 2013, PhRvL, 110, 225002
Cranmer, S. R., Asgari-Targhi, M., Miralles, M. P., et al. 2015, RSPTA, 373, 20140148
Duan, D., He, J., Wu, H., & Verscharen, D. 2020, ApJ, 896, 47
Gershman, D. J., Adolfo, F., Dorelli, J. C., et al. 2017, NatCo, 8, 14719
He, J., Duan, D., Wang, T., et al. 2019, ApJ, 880, 121
He, J., Marsch, E., Tu, C., & Tian, H. 2009, ApJL, 705, L217
He, J., Marsch, E., Tu, C., Yao, S., & Tian, H. 2011, ApJ, 731, 85
He, J., Pei, Z., Wang, L., et al. 2015a, ApJ, 805, 176
He, J., Tu, C., Marsch, E., & Yao, S. 2012, ApJ, 749, 86
He, J., Wang, L., Tu, C., Marsch, E., & Zong, Q. 2015b, ApJL, 800, L31
He, J., Zhu, X., Verscharen, D., et al. 2020, ApJ, 898, 43
He, J., Zhu, X., Yang, L., et al. 2021, ApJL, 913, L14
Hellinger, P., Trávníček, P., Kasper, J. C., & Lazarus, A. J. 2006, GeoRL, 33, L09101
Howes, G. G., Klein, K. G., & Li, T. C. 2017, JPlPh, 83, 705830102
Huang, S., Zhang, J., Sahraoui, F., et al. 2020, ApJL, 897, L3
Jagarlamudi, V., de Wit, T. D., Froment, C., et al. 2021, A&A, 650, A9
Jian, L., Wei, H., Russell, C., et al. 2014, ApJ, 786, 123
Jian, L. K., Russell, C. T., Luhmann, J. G., et al. 2009, ApJL, 701, L105
Jiansen, H., Xingyu, Z., Yajie, C., et al. 2018, ApJ, 856, 148
Klein, K., Alterman, B., Stevens, M., Vech, D., & Kasper, J. 2018, PhRvL, 120, 205102
Klein, K., Verniero, J., Alterman, B., et al. 2021, ApJ, 909, 7
Luo, Q., Zhu, X., He, J., et al. 2022, ApJ, 928, 36
Malaspina, D. M., Ergun, R. E., Bolton, M., et al. 2016, JGRA, 121, 5088
Marsch, E. 2006, LRSP, 3, 1
Mozer, F., Agapitov, O., Bale, S., et al. 2020a, JGRA, 125, e2020JA027980
Mozer, F., Bonnell, J., Bowen, T., Schumm, G., & Vasko, I. 2020b, ApJ, 901, 107
Mozer, F., & Chen, C. 2013, ApJL, 768, L10
Narita, Y. 2018, LRSP, 15, 1
Narita, Y., Nakamura, R., Baumjohann, W., et al. 2016, ApJL, 827, L8
Podesta, J. 2009, ApJ, 698, 986
Ruan, W., He, J., Zhang, L., et al. 2016, ApJ, 825, 58
Sahraoui, F., Goldstein, M., Robert, P., & Khotyaintsev, Y. V. 2009, PhRvL, 102, 231102
Salem, C. S., Howes, G., Sundkvist, D., et al. 2012, ApJL, 745, L9
Santolík, O., Parrot, M., & Lefeuvre, F. 2003, RaSc, 38, 1010
Shi, C., Zhao, J., Huang, J., et al. 2021, ApJL, 908, L19
Sonnerup, B. Ö., & Cahill, L., Jr 1967, JGR, 72, 171
Stansby, D., Horbury, T., Chen, C., & Matteini, L. 2016, ApJL, 829, L16
Stix, T. H. 1992, Waves in Plasmas (New York: Springer Science & Business Media)
Sun, H., Zhao, J., Liu, W., Xie, H., & Wu, D. 2020, ApJ, 902, 59
Swanson, D. G. 2003, Plasma Waves (Boca Raton, FL: CRC Press)
Tong, Y., Vasko, I. Y., Artemyev, A. V., Bale, S. D., & Mozer, F. S. 2019, ApJ, 878, 41
Torrence, C., & Compo, G. P. 1998, BAMS, 79, 61
Vech, D., Martinovic, M. M., Klein, K. G., et al. 2021, A&A, 650, A10
Verniero, J., Larson, D., Livi, R., et al. 2020, ApJS, 248, 5
Verscharen, D., Bourouaine, S., & Chandran, B. D. 2013, ApJ, 773, 163
Verscharen, D., Klein, K. G., & Maruca, B. A. 2019, LRSP, 16, 1
Woodham, L. D., Wicks, R. T., Verscharen, D., et al. 2019, ApJL, 884, L53
Wicks, R., Alexander, R., Stevens, M., et al. 2016, ApJ, 819, 6
Xie, H., & Xiao, Y. 2016, PlST, 18, 97
Yang, L., Zhang, L., He, J., et al. 2017, ApJ, 851, 121
Yoon, P. H. 2017, RvMPP, 1, 4
Zank, G., Nakanotani, M., Zhao, L.-L., Adhikari, L., & Kasper, J. 2020, ApJ, 903, 1
Zhang, Y., Feng, W., Chen, Y., et al. 2012, GeoJI, 191, 1417
Zhao, G., Feng, H., Wu, D., Pi, G., & Huang, J. 2019, ApJ, 871, 175
Zhao, G. Q., Lin, Y., Wang, X., et al. 2020, GeoRL, 47, e2020GL089720
Zhao, J., Wang, T., Dunlop, M., et al. 2018, ApJ, 867, 58
Zhao, L., Zank, G., He, J., et al. 2021, A&A, 656, A3
Zhu, X., He, J., Verscharen, D., & Zhao, J. 2019, ApJ, 878, 48